

Exploring microrotational effects and temperature variations in electroosmotic peristalsis in tapered microchannel

Sidra Batool¹  | Saima Noreen¹  | Ali J. Chamkha²

¹Department of Mathematics, COMSATS University Islamabad, Islamabad, Pakistan

²Kuwait College of Science & Technology, Doha District, Kuwait

Correspondence

S. Noreen, Department of Mathematics, COMSATS University Islamabad, Park Road, Tarlai Kalan, Islamabad 45550, Pakistan.

Email: laurel_lichen@yahoo.com

The current study is based on the effects of microrotational dynamics, microinertial effects, and temperature changes on electroosmotic peristalsis in a tapered microchannel. This has been addressed by an analytical study of heat transfer in the setting of electroosmotic peristaltic flow involving a micropolar fluid, specifically considering a symmetrically tapered channel. The Navier–Stokes equation, the Poisson–Boltzmann equation, the energy equation, and the micropolar fluid model are all included in the mathematical model. On the flow and temperature fields, a thorough parametric analysis is carried out, investigating the impacts of numerous variables, including the micropolar parameter, Prandtl number, Brinkman number, Grashof number, thermal conductivity ratio, and channel aspect ratio. The findings show that peristalsis and electroosmosis both contribute to higher heat transfer rates. Notably, the electroosmotic parameter and Brinkman number have a substantial impact on the distribution of temperature. The micropolar parameter and Brinkman number have a significant effect on the flow and temperature fields. Furthermore, electrokinetic phenomena are crucial in controlling the axial and spin velocities of the micropolar fluid. These findings have significant ramifications for the design and optimization of microfluidic devices in engineering and biomedical applications that employ the electroosmotic peristaltic flow of micropolar fluids.

1 | INTRODUCTION

Peristalsis refers to a wave of progressive contraction traveling along a canal or tube, resulting in a change in cross-sectional area. It has been discovered to serve a role in the physiology of numerous biological systems. Peristalsis facilitates the passage of food through the esophagus, stomach, and intestines in the digestive tract, as well as the movement of urine from the kidneys to the bladder and eventually outside the body in the urinary system. The autonomic nervous system, which regulates the peristaltic motion in these systems, is affected by several variables, such as hormones, medications, and the presence of food or urination in the system. This analysis was first presented by Latham [1]. Several theoretical and experimental investigations were conducted in order to fathom the peristalsis phenomena in ureteral functions. Following Latham's footsteps, Shapiro [2, 3] has investigated the reflux phenomenon from a biological and medical perspective. In addition to its application in biological systems, peristaltic motion has been studied in the context of microfluidic devices. By inducing peristaltic motion through the periodic relaxation and contraction of the walls of a microchannel or

microtube, these systems enable fluid mixing, pumping, and particulate management. Recent research [4–9] relevant to peristaltic flows is scant.

Electroosmotic flow is a phenomenon caused by the interaction between a fluid and an electric field. This effect is vital to fluid mixing and propulsion in microfluidics, where it is of utmost importance. Electroosmosis has been extensively studied [10] in the context of microfluidic devices designed for diverse applications such as chemical analyses, biological assays, and drug delivery systems. In addition, the fabrication of lab-on-a-chip systems for manipulating and transporting samples has utilized electroosmotic flow [11]. Numerous studies [12–16] have investigated the fundamental principles underlying electroosmotic flow and its influence on fluid dynamics and heat transfer in microfluidic channels. In addition, researchers have investigated the relationship between electroosmotic flow and other fluidic phenomena, such as peristalsis. Notably, Chakraborty [17] presented a model that integrated the effects of peristaltic pumping and electroosmosis, casting light on how this interaction can improve peristaltic pumping. In this study, peristalsis and electrokinetic transfer are examined, with an emphasis on their physiological applications. Tripathi and coworkers [18] delved further into the peristaltic motion of a micropolar fluid within a conduit with slip effects and electroosmotic transport. Their findings demonstrated the significant impact of electroosmosis on flow dynamics and heat transfer properties.

A micropolar fluid is a fluid that contains dispersed particles in a viscous medium, with each particle exhibiting random orientations. Eringen [19] introduced the concept of micropolar fluids. These fluids can withstand connected forces, body couplings, and microrotational and micro inertial phenomena. Eringen's initial presentation of his theory of simple micropolar fluids [20] provides a comprehensive examination of the micropolar fluid concept. Ariman et al. [21] have provided a comprehensive overview of micro continuum fluid mechanics, encompassing a variety of physiological fluid flow applications.

Since the inception of the micropolar fluid hypothesis [22–25], few researchers have investigated the peristaltic flow dynamics of these fluids. As a result of their unique properties and potential applications, micropolar fluids are becoming an increasing focus of research in microfluidic devices. Fluids with inherent microstructural characteristics that manifest complex behavior in fluid fluxes are termed micropolar. Due to their importance in chemical engineering, biomedical engineering, and microfluidic systems, the transport of micropolar fluids within microchannels, mainly tapered microchannels, has attracted considerable scholarly interest.

Understanding the mechanisms of peristalsis and electroosmosis in micropolar fluid flow within microchannels has been the subject of numerous studies. Nonetheless, the impact of heat transfer on these mechanisms has yet to be exhaustively investigated. Using simulations and a mathematical model, Prakash et al. [26] investigated the effect of electroosmotic flow on heat transfer within tapered microchannels. Their research revealed that electroosmotic flow in tapered microchannels modifies the blood's heat transfer properties and that electroosmotic pumping increases heat transfer rates. In a distinct study, Narla et al. [27] investigated the thermal behavior of micropolar fluid flow in microchannels driven by electroosmosis and peristalsis. Utilizing a numerical model, they analyzed the effect of various parameters, including the micropolar parameter, electrokinetic parameter, and peristaltic amplitude, on the heat transfer and flow properties of fluids. The incorporation of the microrotation vector is a distinct advantage of the micropolar fluid model compared to other non-Newtonian fluid models [28]; this advantage is unique to the micropolar fluid model. This vector acts as a specific kinematic measure to quantify fluid particle rotation.

Our goal is to examine the interplay between micropolar fluid flow and electroosmosis, peristalsis, and heat transfer in a tapered symmetric channel. To investigate the effects of physical characteristics on heat transfer, such as the electroosmotic parameter, amplitude ratio, Reynolds number, and micropolar parameter, we will construct a mathematical model. The results of their influence on the velocity and temperature distributions are also analyzed. The flow is thought to be driven by peristalsis and an axial electric field. When the zeta potential is less than 25 mV, the Debye–Huckel approximation holds. We perform statistical analysis on a variety of parameters, displaying our findings graphically. The DSolve Mathematica program is used to obtain exact closed-form solutions.

2 | MATHEMATICAL MODEL

2.1 | Flow analysis

In the presence of a thermal effect, the electroosmotic movement in a tapered symmetric regime via peristaltic waves traveling along walls is considered and presented in Figure 1. Wave train stated in Equation (1) moves along the channel

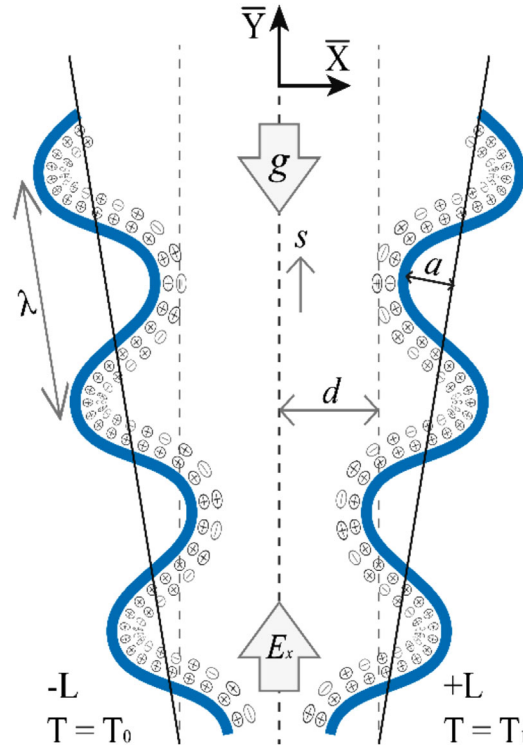


FIGURE 1 Schematic representation of problem.

walls at a fixed speed s to create the peristaltic flow. Let $Y = \pm L$ be left and right walls of channel.

$$\bar{L}(\bar{X}, \bar{t}) = d + \bar{n}(\bar{X} - s\bar{t}) + a \cos \left[\frac{2\pi}{\lambda}(\bar{X} - s\bar{t}) \right] \quad (1)$$

where wavelength is the λ , time is the \bar{t} , wave amplitude is the a , wave speed is the s , dimensional nonuniform parameter is the \bar{n} , and channel width is the $2d$. Temperatures are kept consistent on the left-side wall at T_0 and the right-side wall at T_1 .

2.2 | Governing equations

Fundamental governing equations for micropolar fluid moving steadily under the influence of convective heat transfer in electroosmosis peristaltic pumping through a tapered symmetric channel in the absence of body forces and body couple:

$$\frac{\partial \bar{F}}{\partial \bar{X}} + \frac{\partial \bar{G}}{\partial \bar{Y}} = 0, \quad (2)$$

$$\rho \left(\bar{F} \frac{\partial \bar{F}}{\partial \bar{X}} + \bar{G} \frac{\partial \bar{F}}{\partial \bar{Y}} \right) = \frac{\partial \bar{p}}{\partial \bar{X}} + (\mu + k) \left(\frac{\partial^2 \bar{F}}{\partial \bar{X}^2} + \frac{\partial^2 \bar{F}}{\partial \bar{Y}^2} \right) + k \frac{\partial \bar{w}}{\partial \bar{Y}} + \rho_e E_x + \rho g \lambda (T - T_0), \quad (3)$$

$$\rho \left(\bar{F} \frac{\partial \bar{G}}{\partial \bar{X}} + \bar{G} \frac{\partial \bar{G}}{\partial \bar{Y}} \right) = -\frac{\partial \bar{p}}{\partial \bar{Y}} + (\mu + k) \left(\frac{\partial^2 \bar{G}}{\partial \bar{X}^2} + \frac{\partial^2 \bar{G}}{\partial \bar{Y}^2} \right) - k \frac{\partial \bar{w}}{\partial \bar{X}}, \quad (4)$$

$$\rho \bar{j} \left(\bar{F} \frac{\partial \bar{w}}{\partial \bar{X}} + \bar{G} \frac{\partial \bar{w}}{\partial \bar{Y}} \right) = -2k\bar{w} + k \left(\frac{\partial \bar{G}}{\partial \bar{X}} + \frac{\partial \bar{F}}{\partial \bar{Y}} \right) + \gamma \left(\frac{\partial^2 \bar{w}}{\partial \bar{X}^2} + \frac{\partial^2 \bar{w}}{\partial \bar{Y}^2} \right), \quad (5)$$

$$\rho c_p \left(\bar{F} \frac{\partial \bar{T}}{\partial \bar{X}} + \bar{G} \frac{\partial \bar{T}}{\partial \bar{Y}} \right) = \kappa \left(\frac{\partial^2 \bar{T}}{\partial \bar{X}^2} + \frac{\partial^2 \bar{T}}{\partial \bar{Y}^2} \right) + Q_0 \quad (6)$$

Here, \bar{F} , \bar{G} , \bar{j} , \bar{p} , \bar{w} , μ , T , c_p , κ , Q_0 , α , and k & γ are the velocity along \bar{X} and \bar{Y} direction, microgyration parameter, fluid pressure, microrotation vector, viscosity constant for dynamic fluid, fluid temperature, specific heat at constant pressure, thermal conductivity of fluid, constant heat addition/absorption, coefficient of linear thermal expansion, and viscosity constants for micropolar fluid, respectively.

2.3 | Electrohydrodynamic (EHD)

The Poisson's equation is written as [29]:

$$\nabla^2 \cdot \bar{\Phi} = -\frac{\rho_e}{\varepsilon}, \quad (7)$$

where ρ_e represents density of all ionic charges and ε represents permittivity. The ionic charge density $\rho_e = ez(-n^- + n^+)$, defined in Poisson equation is determined by Boltzmann distribution as:

$$n^\pm = n_0 \text{Exp} \left(\pm \frac{ez}{T_{av} K_B} \Phi \right),$$

where n^- and n^+ represent the number of anion and cation densities, T_{av} is the average temperature, e is the electronic charge, n_0 is the bulk concentration, z is the charge balance, and K_B is the Boltzmann constant. When Debye-Huckel linearization (i.e., $\sinh \Phi \approx \Phi$) is adopted, Poisson-Boltzmann equation becomes:

$$\frac{\partial^2 \Phi}{\partial y^2} = m_e^2 \Phi. \quad (8)$$

where m_e is the electroosmotic parameter. Subject to boundary conditions $\Phi = 1$, at $y = L(x)$ and $\frac{\partial \Phi}{\partial y} = 0$, at $y = 0$, the analytical solution of above equation is obtained as:

$$\Phi(y) = \frac{\cos(m_e y)}{\cos(m_e L)}. \quad (9)$$

2.4 | Transformation and nondimensionalization

The following expressions link the velocities and coordinates in both frames.

$$\begin{aligned} \bar{x} &= \bar{X} - st, \bar{y} = \bar{Y}, \\ \bar{f} &= \bar{F} - s, \quad \bar{g} = \bar{G} \end{aligned} \quad (10)$$

where (\bar{F}, \bar{G}) is the velocity components in fixed frame and (\bar{f}, \bar{g}) is the velocity components in wave frame of reference. Consider the following nondimensional parameters and variables to simplify governing equations.

$$\begin{aligned} x &= \frac{\bar{x}}{\lambda}, y = \frac{\bar{y}}{d}, f = \frac{\bar{f}}{s}, g = \frac{\lambda \bar{g}}{ds}, w = \frac{d\bar{w}}{s}, \Phi = \frac{\bar{\Phi}}{\zeta}, L = \frac{\bar{L}}{d}, \phi = \frac{a}{d}, \delta = \frac{d}{\lambda}, p = \frac{d^2 \bar{p}}{s\lambda\mu}, j = \frac{\bar{j}}{d^2}, \\ R_e &= \frac{\rho s d}{\mu}, \theta = \frac{T - T_0}{T_1 - T_0}, n = \frac{\lambda \bar{n}}{d}, G_r = \frac{d^2 \alpha g (T_1 - T_0)}{\nu s}, p_r = \frac{\mu c_p}{\kappa}, B_r = \frac{Q_0 d^2}{\kappa (T_1 - T_0)}. \end{aligned} \quad (11)$$

where R_e , G_r , p_r , ζ , and δ are Reynolds number, Gharshof number, Parntl number, zeta potential, and wave number, respectively. Employing (10) and (11) in Equations (2-6), we get

$$\frac{\partial f}{\partial x} + \frac{\partial g}{\partial y} = 0, \quad (12)$$

$$R_e \delta \left(f \frac{\partial f}{\partial x} + g \frac{\partial f}{\partial y} \right) = -\frac{\partial p}{\partial x} + \frac{1}{1-R} \left(R \frac{\partial w}{\partial y} + \delta^2 \frac{\partial^2 f}{\partial x^2} + \frac{\partial^2 f}{\partial y^2} \right) + m_e^2 \Phi U_{HS} + G_r \theta, \quad (13)$$

$$R_e \delta^3 \left(f \frac{\partial g}{\partial x} + g \frac{\partial g}{\partial y} \right) = -\frac{\partial p}{\partial y} + \frac{\delta^2}{1-R} \left(-R \frac{\partial w}{\partial x} + \delta^2 \frac{\partial^2 g}{\partial x^2} + \frac{\partial^2 g}{\partial y^2} \right), \quad (14)$$

$$\frac{R_e j \delta (1-R)}{R} \left(f \frac{\partial w}{\partial x} + g \frac{\partial w}{\partial y} \right) = yw + \left(\delta^2 \frac{\partial g}{\partial x} - \frac{\partial f}{\partial y} \right) - \frac{2-R}{M^2} \left(\delta^2 \frac{\partial^2 w}{\partial x^2} + \frac{\partial^2 w}{\partial y^2} \right), \quad (15)$$

$$R_e \delta \left(f \frac{\partial \theta}{\partial x} + g \frac{\partial \theta}{\partial y} \right) = \frac{1}{p_r} \left(\delta^2 \frac{\partial^2 \theta}{\partial x^2} + \frac{\partial^2 \theta}{\partial y^2} \right) + B_r. \quad (16)$$

where $M^2 = \frac{d^2 k(2\mu+k)}{\gamma(\mu+k)}$ is micropolar parameter, $R = \frac{k}{\mu+k}$ is coupling number ($0 \leq R \leq 1$, due to its physical interpretation and the restrictions it represents within the perspective of the model), $U_{HS} = -\frac{E_x \varepsilon \zeta}{\mu s}$ is dimensionless Helmholtz-Smoluchowski velocity and $m_e = dze \sqrt{\frac{2n_0}{\varepsilon T_{av} k_B}}$ is electroosmotic parameter. The governing equations have the following form when the lubrication approximation ($\delta = \frac{d}{\lambda} \simeq 0$) is used:

$$R \frac{\partial w}{\partial y} + \frac{\partial^2 f}{\partial y^2} + (1-R) m_e^2 \Phi U_{HS} + (1-R) G_r \theta = (1-R) \frac{\partial p}{\partial x}, \quad (17)$$

$$\frac{\partial p}{\partial y} = 0, \quad (18)$$

$$-2w - \frac{\partial f}{\partial y} + \left(\frac{2-R}{M^2} \right) \frac{\partial^2 w}{\partial y^2} = 0, \quad (19)$$

$$\frac{\partial^2 \theta}{\partial y^2} + p_r B_r = 0. \quad (20)$$

2.5 | Volume flow rate

In laboratory frame,

$$Q = \int_0^{L(\bar{X}, \bar{t})} \bar{F}(\bar{X}, \bar{Y}, \bar{t}) d\bar{Y} \quad (21)$$

In wave frame the equation become:

$$q = \int_0^{\bar{L}(\bar{x})} \bar{f}(\bar{x}, \bar{y}) d\bar{y} \quad (22)$$

dimensionless mean flows ϑ and H in both frames are given by:

$$\vartheta = H + 1 + nx. \quad (23)$$

where

$$\vartheta = \frac{\bar{Q}}{ds}, H = \frac{q}{ds}. \quad (24)$$

In which

$$H = \int_0^1 f dy. \quad (25)$$

Wall surface in dimensionless form is:

$$L(x) = 1 + nx + \phi \cos 2\pi x, \quad (26)$$

here $\phi = \frac{a}{d}$.

Associated boundary conditions are:

$$f = -1, \text{ at } y = \pm(1 + nx + \phi \cos 2\pi x), \quad (27)$$

$$w = 0, \text{ at } y = \pm(1 + nx + \phi \cos 2\pi x). \quad (28)$$

2.6 | Exact solution

For w , f , and θ , the set of Equations (17–20), subject to boundary conditions (27, 28), are exactly solved. They are

$$\theta = \frac{(L - y)(1 + L(L + y) B_r p_r)}{2L}, \quad (29)$$

$$f = -1 + A_1 + A_2 - \frac{1}{8} G_r (-1 + R) (L^2 - y^2)^2 B_r p_r - U_{HS} + \frac{U_{HS} A_3}{(m_e - M)^2 M (m_e + M)^2} + \frac{L^2 G_r (-1 + R) (M y (M^2 + R \chi) - R \chi \operatorname{Sech}(LM) \sinh(My))}{6LM (M^2 + R \chi) - 6R \chi \tanh(LM)}, \quad (30)$$

$$w = A_4 ((m_e - M)^2 M^2 (m_e + M)^2 \left(\frac{A_5}{A_6} \right) + 2L \cosh(LM) (G_r (m_e - M)^2 (m_e + M)^2 B_r p_r A_7 + 2m_e^2 M^4 U_{HS} A_8)). \quad (31)$$

where $\chi = \frac{M^2}{2-R}$.

Stream function is written as:

$$f = \frac{\partial \psi}{\partial y}, g = -\frac{\partial \psi}{\partial x} \quad (32)$$

using the value $f = \frac{\partial \psi}{\partial y}$ in Equation (30), we can derive the expression for ψ .

Using Equation (25), we can find expression for pressure gradient as:

$$\frac{dp}{dx} = -A_9 \left(3M^4 \left(-L + \frac{5L^3 G_r}{24} - q - \frac{5}{24} L^3 G_r R - \frac{1}{15} L^5 G_r (-1 + R) B_r p_r - LU_{HS} + \frac{U_{HS}}{(m_e - M)^2 M^2 (m_e + M)^2} \left(A_{10} + \frac{A_{11}}{m_e} \right) + A_{12} \right) \right). \quad (33)$$

where the Appendix has values for $A_1 - A_{12}$.

The dimensionless pressure rises per wavelength ΔP_λ is:

$$\Delta P_\lambda = \int_0^1 \frac{\partial p}{\partial x} dx \quad (34)$$

The frictional force $Fric_\lambda$ is written as:

$$Fric_\lambda = -L^2 \int_0^1 \frac{\partial p}{\partial x} dx. \quad (35)$$

3 | VALIDATION OF RESULTS

We contrast our analytical solution for the dimensionless velocity with the outcomes provided in a prior study [30], focusing on a particular scenario to demonstrate the accuracy of our ongoing research. The Helmholtz–Smoluchowski velocity ($U_{HS} = 0$), nonuniform parameter ($n = 0$), electroosmotic ($m_e \rightarrow 0$), and heat transfer effects are neglected in this specific scenario. Comparing our model to the results from ref. [30] is shown in Figure 2. To conduct appropriate

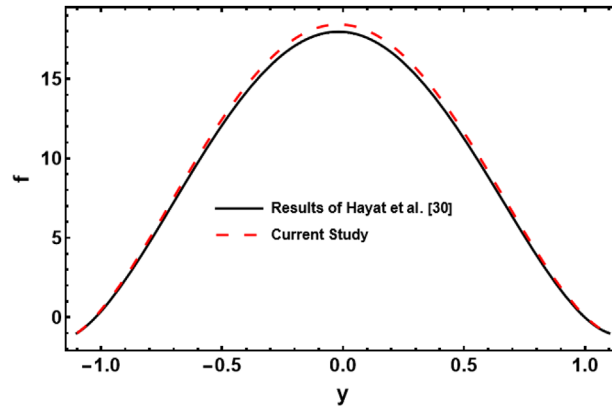


FIGURE 2 A comparison of the axial velocity between the results of the current study's special case and the previous study of Ali and Hayat [30].

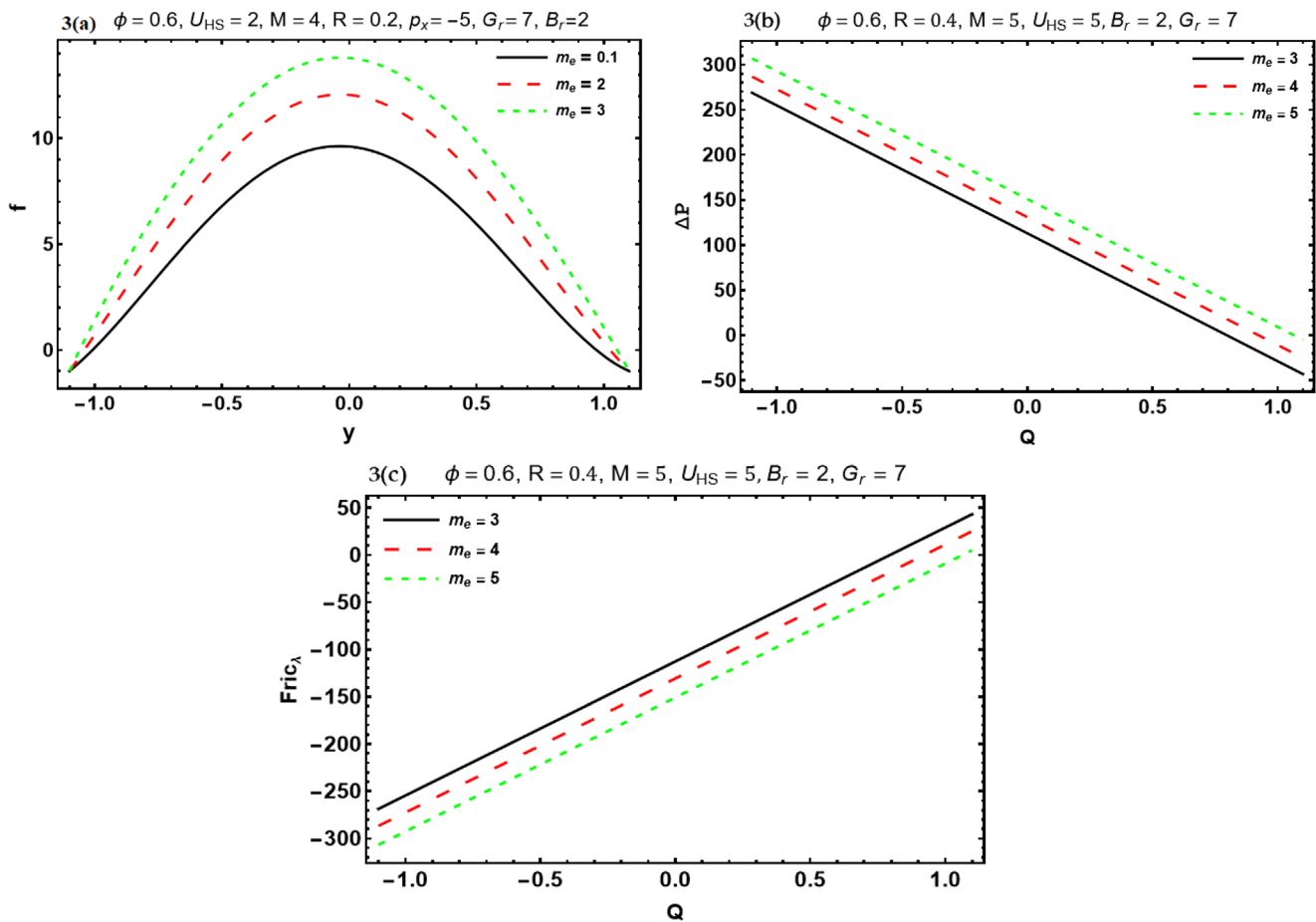


FIGURE 3 Effects of electroosmotic parameters m_e on velocity profile (a), pressure rise (b), and frictional force (c).

comparisons, we have established $U_{HS} = 0$, $m_e = 0.001$, $n = 0$, $B_r = 0$, $p_r = 5$, $M = 10$, $\phi = 0.6$, $R = 0.2$. When the electroosmotic and heat transfer effects are minimal, only hydrodynamic mechanisms control the fluid flow. This illustrates a purely hydrodynamic flow scenario where the velocity profile is not significantly affected by the applied electric field.

When the nonuniform parameter is 0, the electroosmotically regulated peristaltic pumping system has a uniform flow profile. In this case, there are no gradients or spatial variations in the flow characteristics. As a result, the nonuniform parameter does not affect the temperature profile because there are no fluctuations that may cause temperature variances inside the system. Our findings in this case showed excellent agreement with those of [30].

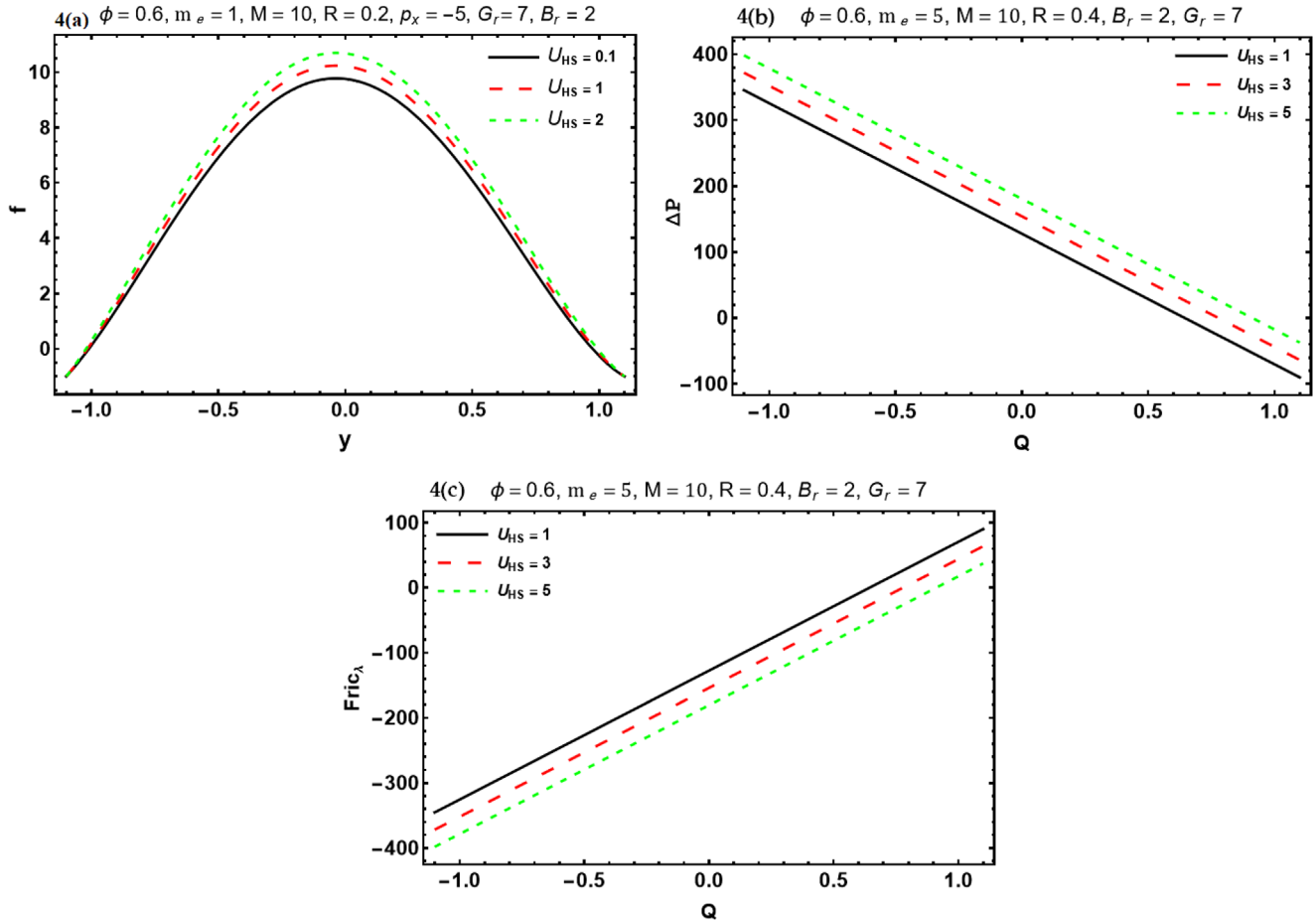


FIGURE 4 Effects of Helmholtz–Smoluchowski velocity U_{HS} on velocity profile (a), pressure rise (b), and frictional force (c).

4 | GRAPHICAL ANALYSIS AND DISCUSSION

The analytical exact solutions are computed and shown using figures to examine how different physical factors impact heat transfer in electroosmotically regulated peristaltic pumping via a tapered symmetric channel. We begin by discussing the parameters physically. Electroosmotic flow is the movement of a liquid caused by an electric field applied over a charged surface. Heat transfer, which can happen because of the energy dissipation associated with the fluid flow and the electric field that promotes the electroosmotic flow, is referred to in electroosmotically regulated peristaltic pumping as the transfer of thermal energy between the fluid and the surroundings. By altering the strength of the electric field that is provided to the channel walls, the fluid flow and the subsequent heat transfer can be managed in electroosmotically regulated peristaltic pumping. It is possible to enhance or suppress fluid flow and the corresponding heat transfer by controlling the electric field, which can be helpful in a variety of applications such as microfluidic devices, lab-on-a-chip systems, and drug delivery systems.

Figure 3a–c show how the electroosmotic parameter affects the velocity profile, pressure rise, and frictional force. The electroosmotic parameter defines the thickness of the EDL (i.e., for $m_e \rightarrow \infty$, the EDL is so thin that it can be physically interpreted that the distribution of charge on the wall surface has no influence on fluid flow. The electroosmotic parameter is usually represented by the zeta potential, which is a measurement of the surface charge density at the fluid–solid interface. The zeta potential controls the size, direction, and speed of the electroosmotic flow. Figure 3a shows impact of electroosmotic parameter on velocity profile. The area of the velocity profile is observed to be widens as m_e is increased, which decreases thickness of EDL. Impact of electroosmotic parameter on pressure differential is displayed in Figure 3b. Based on the pressure difference, three areas are distinguished: the pumping region for $\nabla p > 0$, the co-pumping region for $\nabla p < 0$, and the free pumping region for $\nabla p = 0$. It has been found that as EDL thickness decreases (m_e is increased), pressure differential increased in all pumping zones. Figure 3c represents the influence of electroosmotic parameter on

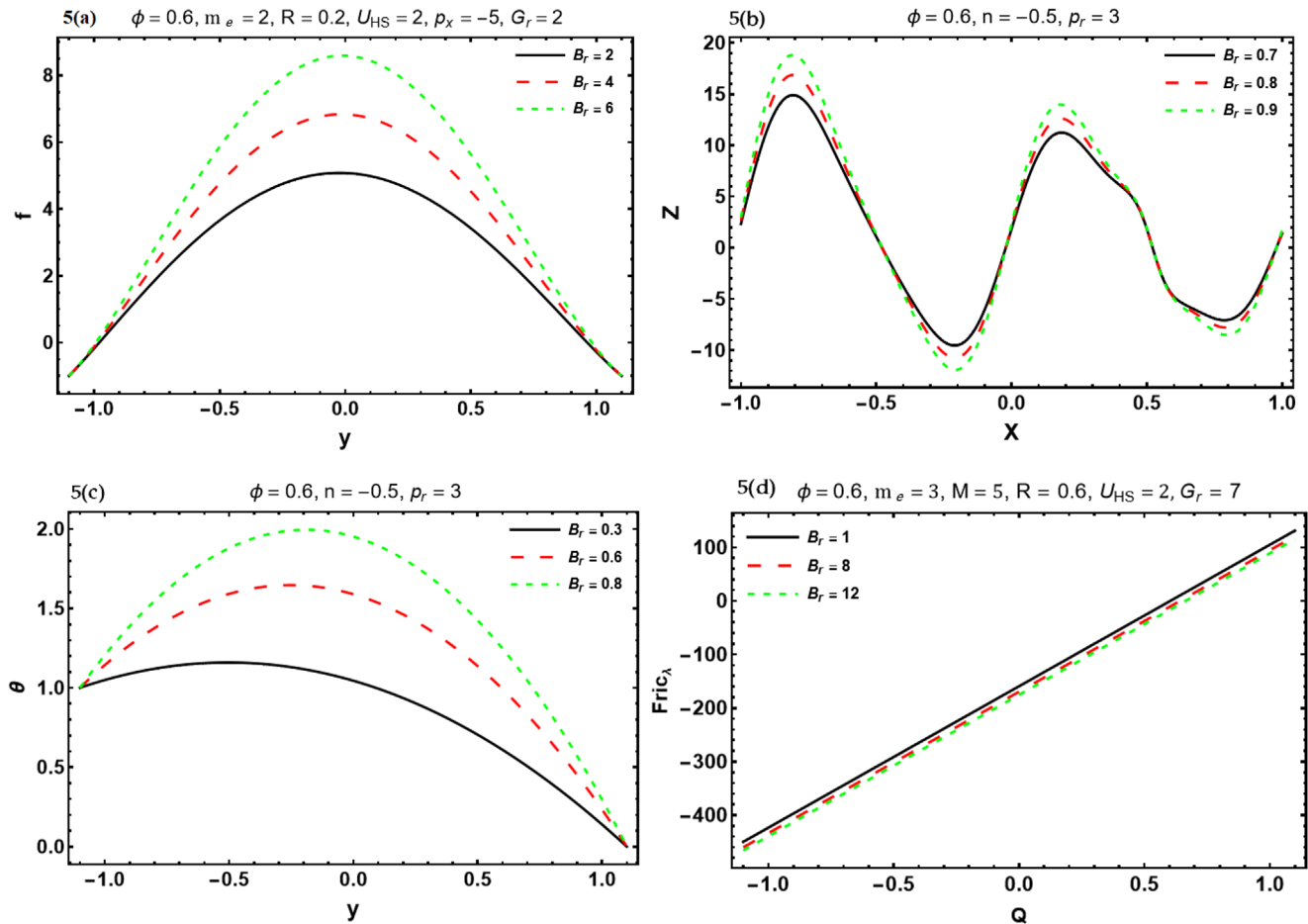


FIGURE 5 Effects of Brinkman number B_r on velocity profile (a), heat transfer coefficient (b), temperature profile (c), and frictional force (d).

frictional forces. It has been observed that the thickness of EDL can be reduced via electroosmotic flow, which can result in a reduction in frictional forces.

From Figure 4a–c, effects of the Helmholtz–Smoluchowski velocity on velocity profile, pressure rise, and frictional force can be seen. Figure 4a illustrates the consequences of Helmholtz–Smoluchowski velocity on the velocity profile. The Helmholtz–Smoluchowski velocity characterizes the effect of an externally applied electric field. It has been observed that velocity rises with increasing electric field strength, showing that electroosmosis may enhance peristaltic flow. Figure 4b shows how pressure difference is affected by Helmholtz–Smoluchowski velocity, and it has been observed for all the pumping regions that pressure differential rises with increasing electric field strength. Figure 4c shows that the frictional forces are reduced when the electric field strength and Helmholtz–Smoluchowski velocity increases.

Through Figure 5a–d, influences of Brinkman number B_r on velocity profile, heat transfer coefficient, temperature profile, and frictional force are explored. Physically, it represents the proportion of inertial effects to viscous dissipation in the flow. A low Brinkman number indicates a dominant role for viscous forces, which results in limited and slower flow characteristics. On the other side, a high Brinkman number shows that inertial effects predominate, leading to faster, less limited flow characteristics. Figure 5a illustrates the impact of Brinkman number on velocity profile and it is found that the velocity rises with an increase in Brinkman number. It has been observed that the temperature profile curve is upwardly concave. The behavior of the heat transfer coefficient is depicted in Figure 5b. The increased viscous dissipation associated with higher Brinkman numbers tends to slow down the flow within the channels. Consequently, compared to circumstances where convection predominates, the heat transfer coefficient tends to be increased. Figure 5c indicates that a rise in temperature profile is caused by Brinkman numbers with higher values. A greater Brinkman number signifies that the conductive forces are superior to the viscous forces. Therefore, a rise in B_r generally results to improved fluid

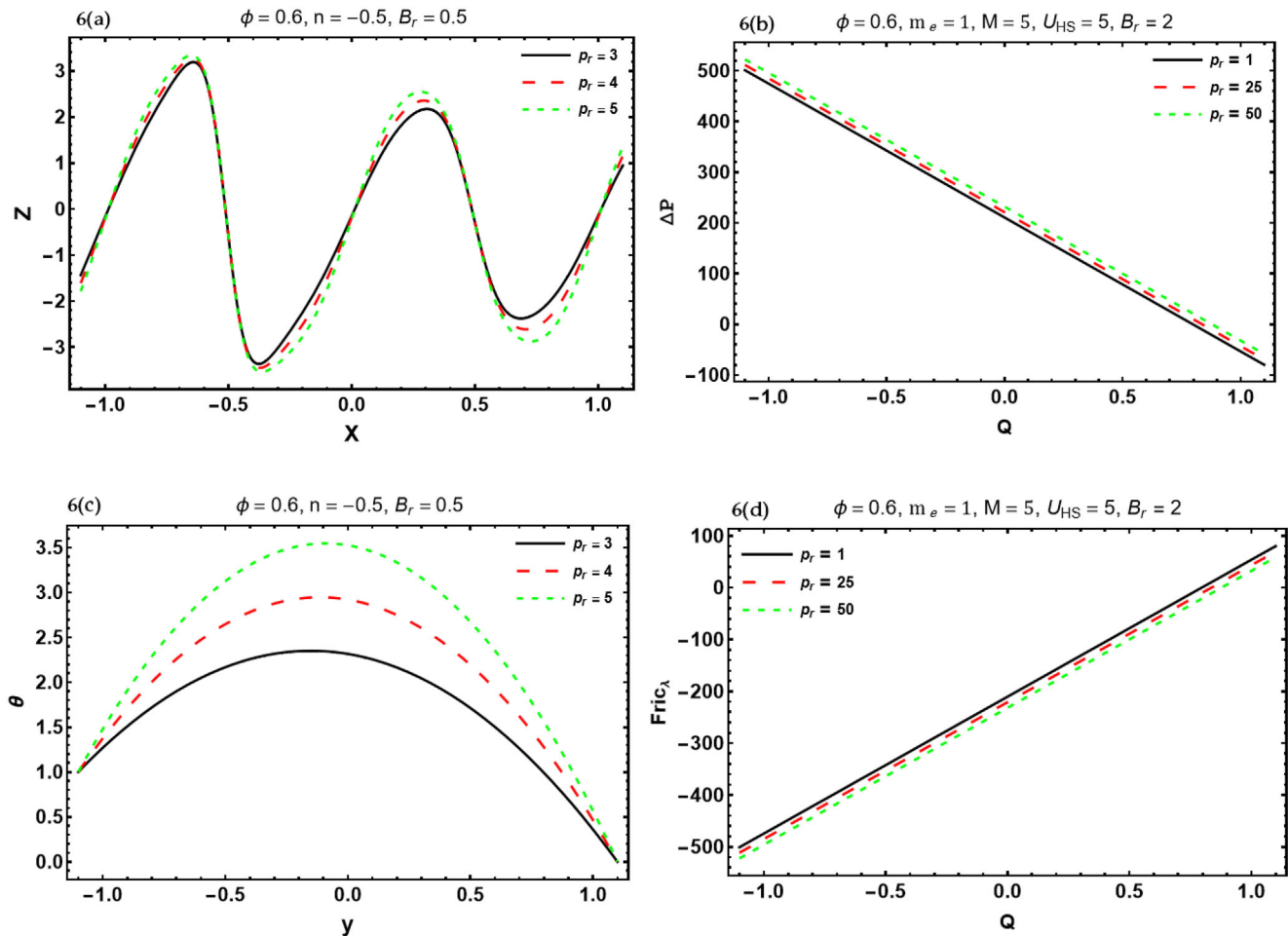


FIGURE 6 Effects of Prandtl number P_r on heat transfer coefficient (a), pressure rise (b), temperature profile (c), and frictional force (d).

mobility and higher convective heat transfer. This may result in a greater temperature profile inside the tapered channel. Figure 5d shows the minor decrease in the friction force with an increase in Brinkman number.

Figure 6a–d illustrate the effects of Prandtl number P_r on heat transfer coefficient, pressure rise, temperature profile, and frictional force. Physically, it describes how effectively temperature changes are distributed or diffused in a fluid. Better heat conduction results from a fluid's tendency to dissipate temperature gradients more quickly due to its higher thermal diffusivity. To examine the effects, three different Prandtl number values are selected. Figure 6a shows a slight change in heat transfer coefficient for increasing Prandtl number. Figure 6b is displayed to show the effects on pressure and it has been found that pressure rise slightly increased with an increase in P_r . Figure 6c shows how the Prandtl number affects temperature distributions. The fluid is thought to have a lower thermal diffusivity compared to its momentum diffusivity if the Prandtl number is larger. As a result, a rise in P_r may result in less thermal diffusion and a smoother temperature profile inside the tapered channel. It is obvious that as the Prandtl number rises, the temperature rises as well. Figure 6d represents the effect of P_r on frictional force. It has been observed that friction slightly decreases when the Prandtl number increases.

To examine the influences of nonuniform parameters on temperature profile, heat transfer coefficient, velocity profile, and pressure rise, Figure 7a–d have been constructed. Physically, the nonuniform parameter affects how the peristaltic waves in the channel are shaped. It determines how much of nonuniformity is brought on by the tapered geometry of the channel cross-section. Figure 7a shows how nonuniform parameters affect temperature distributions. With an increase in the nonuniform parameter, it has been noted that temperature increases. Rising heat transfer coefficient with increasing nonuniform parameter is observed in Figure 7b. The velocity is observed to be increased for an increase in nonuniform parameter, shown in Figure 7c. The influence on pressure rise is displayed through Figure 7d. For an increase in nonuniform parameter, the pressure rise is observed to be increased in pumping region.

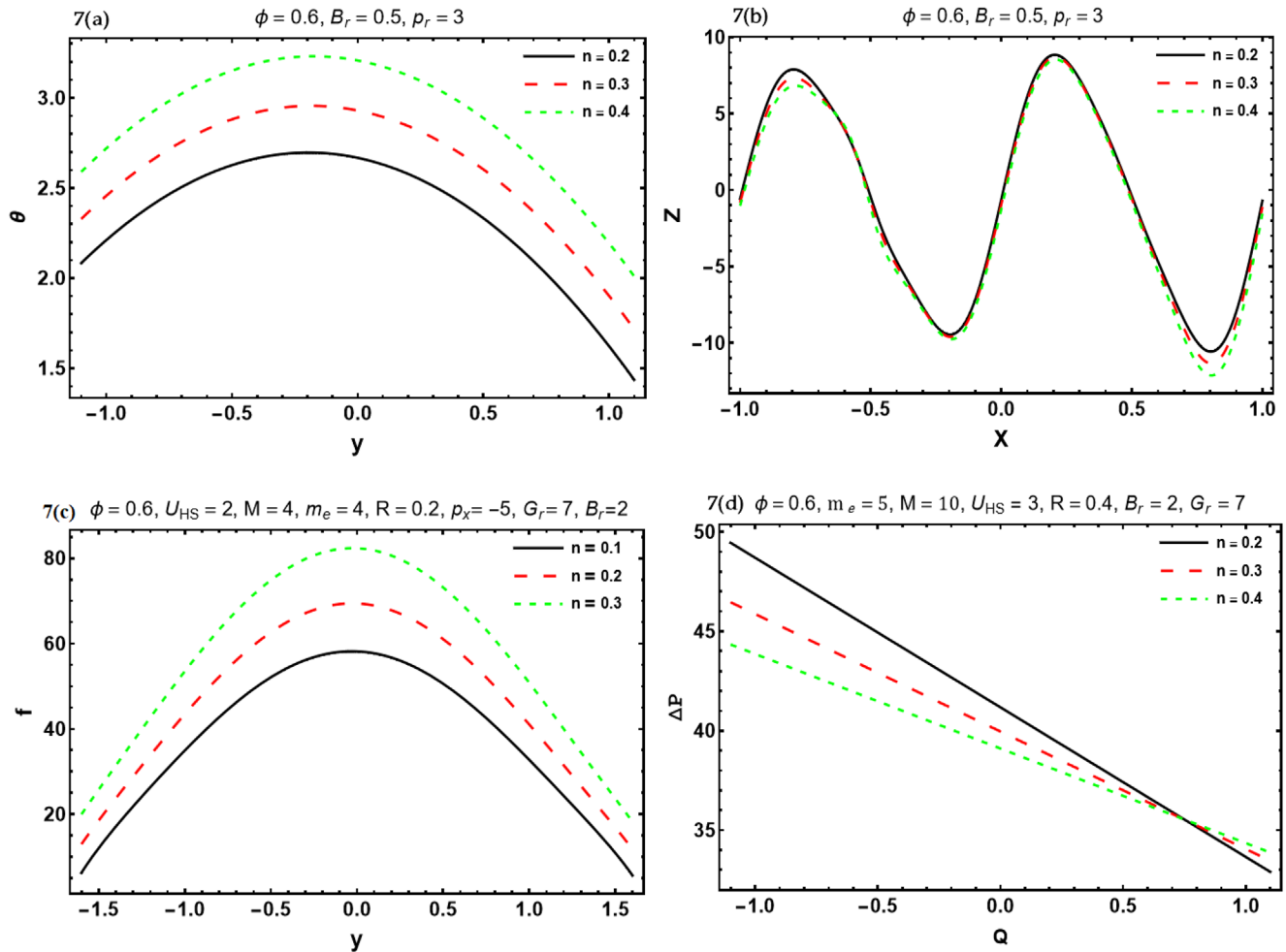


FIGURE 7 Effects of nonuniform parameters n on temperature profile (a), heat transfer coefficient (b), velocity profile (c), and pressure rise (d).

It is well known that the trapping phenomena involve the creation of a fluid bolus that circulates and moves with the wave speed in the wave frame. Studying the streamline's pattern is more essential because the flux of fluid or volumetric flow rate down the line connecting any two points is determined by the difference between the values of the stream function at those two points. Here, we provided some significant findings using Figures 8–10 to illustrate how different parameters affect streamlines. The impact of Brinkman numbers B_r and Grashof numbers Gr on streamlines are illustrated through Figures 8 and 9. It has been found that the size of bolus increases for an increasing magnitude of both B_r and Gr . Figure 10 shows how the symmetric channel's nonuniformity affects the fluctuation of streamlines. We found that the size of trapped bolus slightly increases when the nonuniform parameter n is increased. With an increase in channel length, the bolus size also grows.

5 | CONCLUSION

This study sheds light on heat transfer dynamics by revealing the intricate interaction between electroosmotic and peristaltic effects in micropolar fluid flow within tapered symmetric channels. The findings shed light on controllable flow and heat transfer mechanisms and hold promise for diverse microfluidic applications.

1. The distribution of velocities is significantly affected by both the electric field strength and the electroosmotic parameter, which represents the thickness of the electric double layer (EDL). Flow characteristics are also heavily influenced

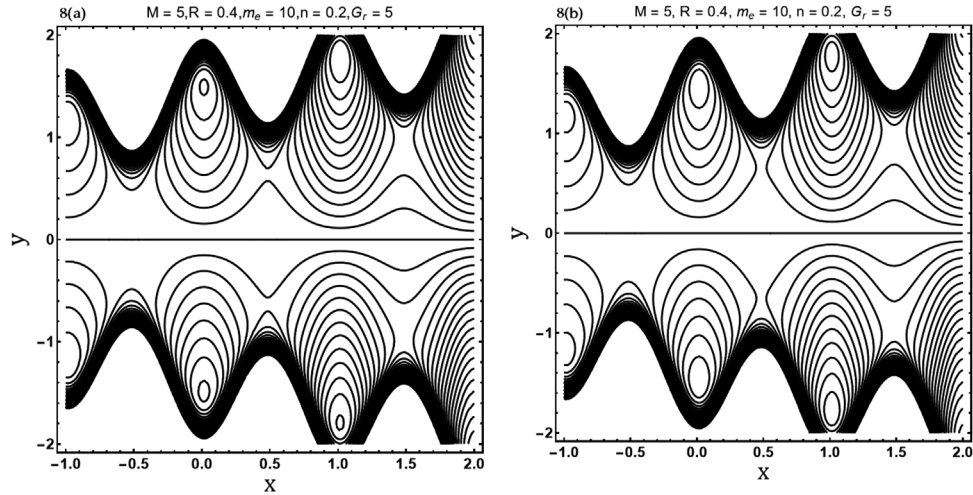


FIGURE 8 Streamlines at $B_r = 5$ and $B_r = 7$.

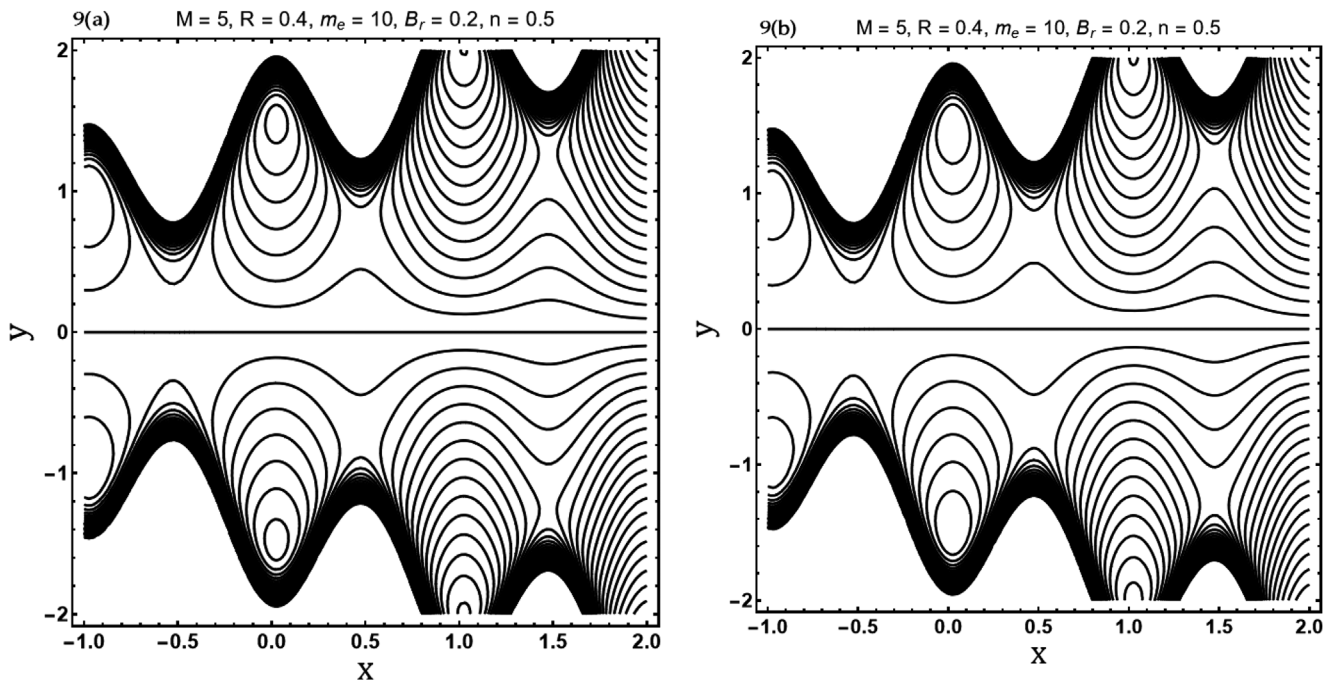


FIGURE 9 Streamlines at $G_r = 3$ and $G_r = 7$.

by the Grashof number and the Brinkman number, with greater values of these parameters typically resulting in higher velocities.

2. High-pressure differentials are typically generated by electric fields that are stronger or have a more significant Grashof number. Temperature profiles with larger increases in β and P_r indicate more efficient convective heat transfer. Notably, though, a rise in the nonuniform parameter can also be blamed for a steeper temperature profile.
3. In addition to the nonuniform parameter and the Brinkman number, the Grashof number also plays a role in determining the bolus's size and the frequency with which bolus spots occur. Bigger bolus sizes and more trapping phenomena occur when these parameters have significantly larger values.

Heat transfer is affected by several physical elements, including electro-osmotic flow, electric field strength, fluid dynamics, and heat exchange, within the setting of electro osmotically driven peristaltic pumping through a tapering symmetric channel. These results suggest that the adjustment of electric field strength can efficiently govern both fluid

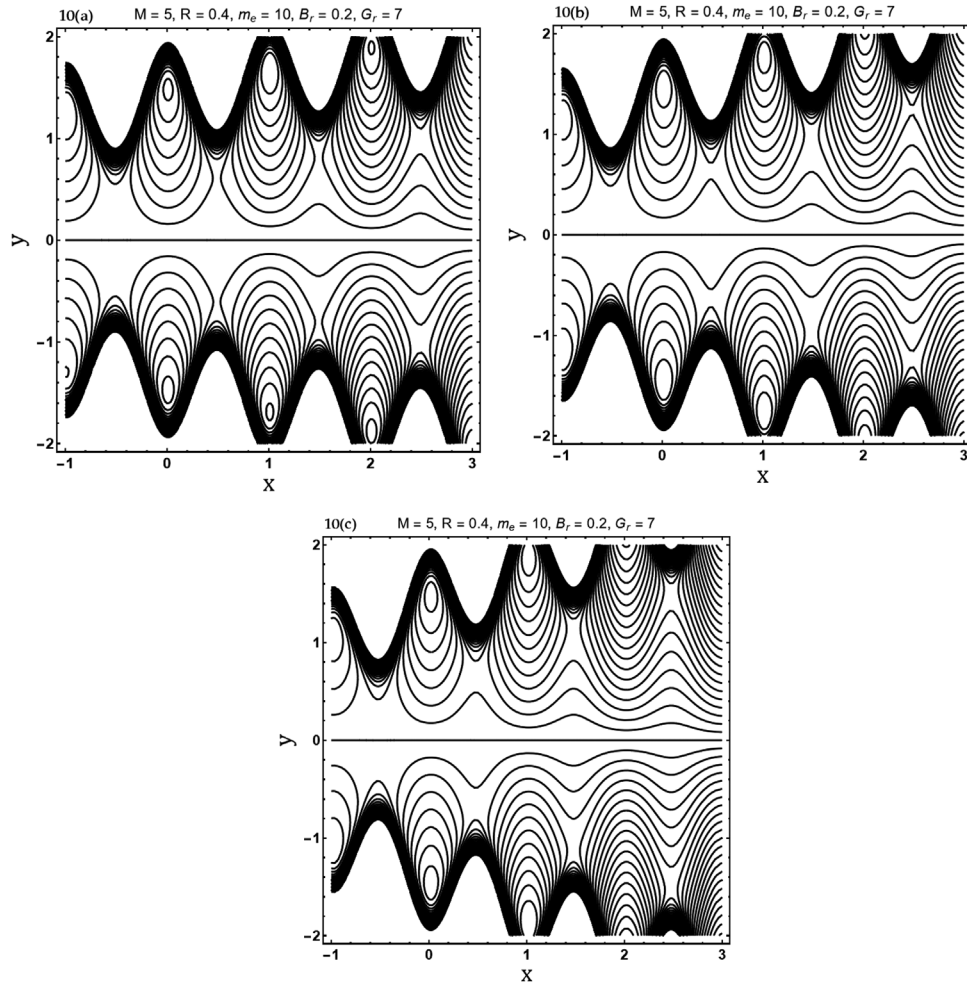


FIGURE 10 Streamlines at $n = 0.2$, $n = 0.3$, and $n = 0.4$.

flow and heat transfer dynamics, which has significant implications for possible applications in microfluidic devices, lab-on-a-chip systems, and drug delivery techniques.

NOMENCLATURE

a	amplitude of wave
B_r	Brinkman number
c_p	specific heat
d	half of channel width
e	electron charge
E_x	external electric field
g	gravity
G_r	Grashof number
(\bar{f}, \bar{g})	velocity components in laboratory frame
(\bar{F}, \bar{G})	velocity components in wave frame
H	mean flow in wave frame
j	micro-gyration parameter
K_B	Boltzmann constant
κ	thermal conductivity
L	wall of channel
$\mu, k, \alpha, \beta, \gamma$	material constants

M	micropolar parameter
m_e	electroosmotic parameter
\bar{n}	dimensional nonuniform parameter
n^\pm	positive and negative ions
P_r	Prandtl number
p	fluid pressure
∇p_λ	pressure rise per wavelength
q	volume flow rate in wave frame
Q	volume flow rate in laboratory frame
\bar{Q}	time averaged flow
R	coupling number
R_e	Reynolds number
s	wave speed
T^*	period
T_{av}	average temperature
T_0, T_1	temperatures at left and right-side wall
U_{HS}	Helmholtz–Smoluchowski velocity
V	velocity vector
w	microrotation vector
z	valence of ions
(\bar{x}, \bar{y})	coordinate axes in wave frame
(\bar{X}, \bar{Y})	coordinate axes in laboratory frame
λ	wavelength
ψ	stream function
ϕ	phase difference
ϑ	mean flow in laboratory frame
ζ	zeta potential
Φ	electric potential
ε	permittivity
ρ	fluid density
ρ_e	density of total ionic charge

ACKNOWLEDGMENTS

The authors have nothing to report.

ORCID

Sidra Batool  <https://orcid.org/0009-0008-6478-8518>

Saima Noreen  <https://orcid.org/0000-0002-7689-304X>

REFERENCES

- [1] Latham, T.W.: Fluid motions in a peristaltic pump. Doctoral Dissertation, Massachusetts Institute of Technology (1966)
- [2] Shapiro, A.H.: Pumping and retrograde diffusion in peristaltic waves. In Proceedings of a Workshop on Ureteral Reflux in Children, National Academy of Sciences, Washington, DC, November 1967
- [3] Shapiro, A.H., Jaffrin, M.Y., Weinberg, S.L.: Peristaltic pumping with long wavelengths at low Reynolds number. *J. Fluid Mech.* 37(4), 799–825 (1969)
- [4] Mekheimer, K.S.: Effect of the induced magnetic field on peristaltic flow of a couple stress fluid. *Phys. Lett. A* 372(23), 4271–4278 (2008)
- [5] Abd Elmaboud, Y., Mekheimer, K.S., Abdellateef, A.I.: Thermal properties of couple-stress fluid flow in an asymmetric channel with peristalsis. *J. Heat Transf.* 135(4), 044502 (2013)
- [6] Mekheimer, K.S., Hasona, W.M., Abo-Elkhair, R.E., & Zaher, A.Z.: Peristaltic blood flow with gold nanoparticles as a third grade nanofluid in catheter: application of cancer therapy. *Phys. Lett. A* 382(2-3), 85–93 (2018)
- [7] Elmaboud, Y.A., Mekheimer, K.S., Emam, T.G.: Numerical examination of gold nanoparticles as a drug carrier on peristaltic blood flow through physiological vessels: cancer therapy treatment. *BioNanoScience* 9, 952–965 (2019)
- [8] Abo-Elkhair, R.E., Bhatti, M.M., Mekheimer, K.S.: Magnetic force effects on peristaltic transport of hybrid bio-nanofluid (AuCu nanoparticles) with moderate Reynolds number: an expanding horizon. *Int. Commun. Heat Mass Transf.* 123, 105228 (2021)

- [9] Gangavathi, P., Jyothi, S., Reddy, M.S., Reddy, P.Y.: Slip and hall effects on the peristaltic flow of a Jeffrey fluid through a porous medium in an inclined channel. *Mater. Today: Proc.* 80, 1970–1975 (2023)
- [10] Haeberle, S., Zengerle, R.: Microfluidic platforms for lab-on-a-chip applications. *Lab Chip* 7(9), 1094–1110 (2007)
- [11] Siddiqui, A.A., Lakhtakia, A.: Non-steady electro-osmotic flow of a micropolar fluid in a microchannel. *J. Phys. A Math. Theor.* 42(35), 355501 (2009)
- [12] Siddiqui, A.A., Lakhtakia, A.: Steady electro-osmotic flow of a micropolar fluid in a microchannel. *Proc. R. Soc. A: Math. Phys. Eng. Sci.* 465(2102), 501–522 (2009)
- [13] Nithi Arasu, P., Eng, P.F.: Numerical modelling of heat generated by electroosmotic flows in micro-channels (2009)
- [14] Siddiqui, A.A., Lakhtakia, A.: Debye-Hückel solution for steady electro-osmotic flow of micropolar fluid in cylindrical microcapillary. *Appl. Math. Mech.* 34, 1305–1326 (2013)
- [15] Ding, Z., Jian, Y., Yang, L.: Time periodic electroosmotic flow of micropolar fluids through microparallel channel. *Appl. Math. Mech.* 37(6), 769–786 (2016)
- [16] Ramesh, K., Prakash, J.: Thermal analysis for heat transfer enhancement in electroosmosis-modulated peristaltic transport of Sutterby nanofluids in a microfluidic vessel. *J. Therm. Anal. Calorim.* 138, 1311–1326 (2019)
- [17] Chakraborty, S.: Augmentation of peristaltic microflows through electro-osmotic mechanisms. *J. Phys. D Appl. Phys.* 39(24), 5356 (2006)
- [18] Chaube, M.K., A. Yadav, D. Tripathi, O. Anwar Bég. Electroosmotic flow of biorheological micropolar fluids through microfluidic channels. *Korea-Aust. Rheol. J.* 30, 89–98 (2018)
- [19] Eringen, A.C.: Simple microfluids. *Int. J. Eng. Sci.* 2(2), 205–217 (1964)
- [20] Eringen, A.C.: Theory of micropolar fluids. *J. Math. Mech.* 1–18 (1966)
- [21] Ariman, T.T.N.D., Turk, M.A., Sylvester, N.D.: Applications of micro continuum fluid mechanics. *Int. J. Eng. Sci.* 12(4), 273–293 (1974)
- [22] SrinivasAcharya, D., Mishra, M., Rao, A.R.: Peristaltic pumping of micropolar fluid in a tube. *Acta Mech.* 161(3), 165–178 (2003)
- [23] Bhargava, R., Sharma, S., Takhar, H.S., Beg, T.A., Bég, O.A., Hung, T.K.: Peristaltic pumping of micropolar fluid in porous channel-model for stenosed arteries. *J. Biomech.* (39), S649 (2006)
- [24] Pandey, S.K., Tripathi, D.: A mathematical model for peristaltic transport of micro-polar fluids. *Appl. Bionics Biomech.* 8(3-4), 279–293 (2011)
- [25] Asha, S.K., Deepa, C.K.: Entropy generation for peristaltic blood flow of a magneto-micropolar fluid with thermal radiation in a tapered asymmetric channel. *Results Eng.* 3, 100024 (2019)
- [26] Prakash, J., Ramesh, K., Tripathi, D., Kumar, R.: Numerical simulation of heat transfer in blood flow altered by electroosmosis through tapered micro-vessels. *Microvasc. Res.* 118, 162–172 (2018)
- [27] Narla, V.K., Tripathi, D., Bhandari, D.S.: Thermal analysis of micropolar fluid flow driven by electroosmosis and peristalsis in microchannels. *Int. J. Ambient Energy* 43(1), 8193–8205 (2022)
- [28] Fusi, L., Farina, A., Saccomandi, G.: Linear stability analysis of the Poiseuille flow of a stratified non-Newtonian suspension: application to microcirculation. *J. Non-Newton. Fluid Mech.* 287, 104464 (2021)
- [29] Chakraborty, S.: Electroosmotically driven capillary transport of typical non-Newtonian biofluids in rectangular microchannels. *Anal. Chim. Acta* 605(2), 175–184 (2007)
- [30] Ali, N., Hayat, T.: Peristaltic flow of a micropolar fluid in an asymmetric channel. *Comput. Math. Appl.* 55(4), 589–608 (2008)

How to cite this article: Batool, S., Noreen, S., Chamkha, A.J.: Exploring microrotational effects and temperature variations in electroosmotic peristalsis in tapered microchannel. *Z Angew Math Mech.* , e202300779 (2024). <https://doi.org/10.1002/zamm.202300779>

APPENDIX

Below, we present the values of constants that appear in Equations (28–32)

$$A_1 = \frac{(-1 + R) \left(M^2 \left(\left(G_r - 2 \frac{dp}{dx} \right) (-3L^3 + 3Ly^2) - 2G_r y^3 \right) + 6LR \frac{dp}{dx} (L^2 - y^2) \chi \right)}{12LM^2},$$

$$A_2 = \frac{L(-1 + R) R \chi \frac{dp}{dx} (-\cot h(LM) + \cos h(My) \csc h(LM))}{M^3},$$

$$A_3 = MR \left((m_e^2 - M^2)^2 + (-3m_e^2 + M^2) (-1 + R) \chi \right) - (-1 + R) (M \sec h(Lm_e) + M^2 R \chi - m_e^2 (2M^2 + 3R \chi)) \cos h(m_e y) + m_e (m_e^2 - M^2) (m_e^2 - M^2 - R \chi)$$

$$\begin{aligned}
& (L \sin h(Lm_e) - y \sin h(y m_e)) m_e^2 R \chi \cot h(LM) (L(m_e^2 - M^2) - 2m_e \tan h(Lm_e)) \\
& m_e^2 R \chi \cos h(My) \csc h(LM) (L(-m_e^2 + M^2) + 2m_e \tan h(Lm_e)), \\
A_4 = & \frac{\cos h(2LM) + \sin h(2LM)}{(-1 + \cos h(4LM) + \sin h(4LM)) L(m_e - M)^2 M^4 (m_e + M)^2} (-1 + R) \chi, \\
A_5 = & \sin h(2LM) (LM \left(6G_r + (M^2 + R\chi) \left(6L \frac{dp}{dx} y - G_r (L^2 + 3Ly - 3y^2) \right) \right)) \cos h(LM) \\
& - 2LG_r M (3 + L^2 (M^2 + R\chi)) \cos h(yM) + 3R \left(L^2 G_r + L \left(G_r - 2 \frac{dp}{dx} \right) y - G_r y^2 \right) \chi \sin h(LM), \\
A_6 = & (3LM (M^2 + R\chi) \cos h(LM) - 3R\chi \sin h(LM)) + 2L^2 \left(G_r - 2 \frac{dp}{dx} \right) \cos h(LM) \sin h(My), \\
A_7 = & (y (6 + M^2 (-L^2 + y^2)) \sin h(LM) - 6L \sin h(My)), \\
A_8 = & \sec h(Lm_e) \sin h(LM) ((m_e^2 - M^2) y \cos h(m_e y) - 2m_e \sin h(y m_e)) \\
& + \sin h(My) (L(-m_e^2 + M^2) + 2m_e \tan h(Lm_e)), \\
A_9 = & \frac{1}{L(-1 + R) (3R\chi + L^2 (M^4 + M^2 R\chi) - 3LMR\chi \cot h(LM))}, \\
A_{10} = & L(-m_e^2 M + M^3)^2 (-1 + 2R) + L(m_e^4 - 5m_e^2 M^2 + 2M^4) (-1 + R) R\chi \\
A_{11} = & (-1 + R) (-((m_e^2 - M^2) (L^2 m_e^4 M^2 - m_e^2 (-2 + L^2 M^2) (M^2 + R\chi) - 2(M^4 + M^2 R\chi))) \tan h(Lm) \\
& + L m^3 M R \chi \cot h(LM) (L(-m_e^2 + M^2) + 2m_e \tan h(Lm_e))), \\
A_{12} = & \frac{L^2 G_r (-1 + R)}{6LM(M^2 + R\chi) - 6R\chi \frac{dp}{dx} \tan h(LM)} \left(\frac{L^2 M^3}{2} + \frac{1}{2} L^2 M R \chi + \frac{R\chi (-1 + \sec h(LM))}{M} \right).
\end{aligned}$$